

Numerical investigation of shallow wake behind a patch of rigid emergent vegetation*

Jian Wang¹, Jing-xin Zhang^{1,2}, Dong-fang Liang³, Lian Gan⁴

1. School of Naval Architecture, Ocean and Civil Engineering, Shanghai Jiao Tong University, Shanghai 200240, China

2. Key Laboratory of Hydrodynamics (Ministry of Education), Shanghai Jiao Tong University, Shanghai 200240, China

3. Department of Engineering, University of Cambridge, Cambridge CB2 1PZ, UK

4. Department of Engineering, Durham University, DH1 3LE, UK

(Received, Revised, Accepted, Published online)

©China Ship Scientific Research Center 2019

Abstract: The shallow water flow through and around a patch of rigid emergent vegetation was investigated numerically. The mean flow field and turbulent structures were studied, especially their dependence on the solid volume fraction (SVF) of the patch and the bed friction. Two streamwise velocity scales, U_{1s} at the starting point of the steady wake and U_{1e} at the downstream end of the steady wake, and the length of the steady wake L_1 were used to describe the steady wake behind the patch. U_{1s} was found to be related to SVF only. However, U_{1e} and L_1 were influenced by both the SVF and the wake stability parameter S . For a sparse patch, U_{1e} was equal to U_{1s} , and L_1 decreased with the increase of S . For a mid-dense patch, U_{1e} was always smaller than U_{1s} , and it increased with S and gradually approached U_{1s} . The increase of U_{1e} reduced the lateral velocity difference between the flows inside and outside the wake, which resulted in the increase of L_1 . For a highly-dense patch, U_{1e} and L_1 did not increase unless S was larger than a critical value. A new parameter, r , was proposed to represent the development rate of the steady wake. The numerical results showed that r increased monotonously with S for mid-dense patches.

Key words: shallow water, vegetated flow, wake, bed friction

Introduction

Aquatic vegetation in open channels plays a significant role in providing a wide range of ecosystem services. It promotes biodiversity in rivers by providing food and habitats and improves water equality by producing oxygen and taking up nutrients^[1]. Further, by altering hydrodynamic conditions, such as flow velocity^[2-4], turbulent structure and mass mixing^[5, 6], vegetation can change sediment deposition and erosion, which controls the bed morphology^[7]. Aquatic plants change the flow field in different scales, ranging from individual branches and leaves on a single plant to a cluster of plants, called canopy or meadow^[8, 9].

The configuration of a finite patch of vegetation, which has a smaller length and width than the channel width, is widespread in the environment^[10]. Hence, the hydrodynamics of flow associated with a patch of emergent vegetation, such as reeds, has received considerable scientific attention in recent years^[11]. Circular cylinders piercing the water surface are commonly used to model rigid emergent vegetation because they have a good approximation of the stems^[12].

A great deal of previous research into the flow past a patch of cylinders has focused on the solid volume fraction (SVF). Ball, et al.^[13] measured the velocity vector fields with the flow around pile groups using particle tracking velocimetry. Downstream of the obstacle, a low-velocity near-wake zone without transverse velocity which was followed by an unstable far wake was observed. Zong & Nepf^[12] investigated the wake structure behind an array of cylinders. The von Karman vortex street was found to start at some distance downstream the porous obstruction in their experiments. The wake region from the trailing edge

* Project supported by the National Key R&D Program of China (Grant No. 2019YFB1503700).

Biography: Jian Wang (1992-), Male, Ph. D. Candidate, E-mail: abcr114@sjtu.edu.cn

Corresponding author: Jing-xin Zhang, E-mail: zhangjingxin@sjtu.edu.cn

of the obstruction to the point where the wake oscillation occurs is called the steady wake. In this region, the streamwise velocity was believed to be roughly constant [14], which was defined as U_1 . In the experiments of Zong & Nepf [12], a constant U_1 was also observed for a sparse patch. However, recent evidence suggested that U_1 decreased along the steady wake for a dense patch [15]. The length of the steady wake, L_1 , is determined by the growth of the two separated shear layers (SSLs) generated at the shoulders of the patch. As the shear strength of the SSLs is dependent on the velocity difference between the steady wake and the flow outside the wake, a correlation between L_1 and U_1 was proposed [14, 12].

The magnitude of U_1 and the formation of the von Karman vortex street behind the steady wake are closely related to SVF. Zong & Nepf [12] reported that U_1 was a function of SVF only. Nicolle & Eames [16] found that the vortex street only occurred when $SVF > 0.05$. Several studies have confirmed that the presence of coherent structures in shallow water flows is associated with the shear instability [17, 18]. The flow patterns in the wake have been found to depend mainly on a shallow wake stability parameter, $S = C_f D/H$, which characterizes the bed friction [19–21]. C_f is a quadratic-law friction coefficient, D is the obstruction diameter, and H is the water depth. Chu & Babarutsi [22] concluded that bed friction exerted a stabilizing force on the large-scale turbulent structures. The vortex street behind a solid body may be suppressed by strong bed friction when $S > 0.20$. Indeed, both the steady wake characteristics and the turbulent structures behind a patch of cylinders are associated with bed friction. However, a systematic understanding of how bed friction affects the wake behind the patch is still lacking. Considering that the shallow water conditions (for very shallow water depth) are not easy to achieve in laboratories, and that the measurements within the patch are practically difficult, numerical investigations are conducted in this study, with the effect of bed friction varied by changing the water depth.

The paper is structured as follows. In Section 1, the numerical formulation and the study cases are described. The simulation results are analyzed and interpreted in Section 2. The correlation between bed friction and steady wake is discussed in Section 3. The general conclusions are presented in Section 4.

1. Methods

1.1 Numerical model

Motivated by the hydrostatic assumption in traditional shallow water flow model, the total pressure is split into the hydrostatic component $p_h =$

$\rho g(\eta - z)$ and the non-hydrostatic component p_n in this model. η is the free surface elevation above the datum, which needs to be solved in the simulations. The vertical coordinate z is transformed into the σ coordinate to adapt to the changing η and uneven bed [23]. After taking the Reynolds average, the 3D governing equations are rewritten in a conservative form as follows:

$$\frac{\partial \eta}{\partial t} + \frac{\partial Hu}{\partial x} + \frac{\partial Hv}{\partial y} + \frac{\partial H\tilde{w}}{\partial \sigma} = 0 \quad (1)$$

$$\begin{aligned} & \frac{\partial Hu}{\partial t} + \frac{\partial Huu}{\partial x} + \frac{\partial Huv}{\partial y} + \frac{\partial Hu\tilde{w}}{\partial \sigma} \\ & = -gH \frac{\partial \eta}{\partial x} - \frac{H}{\rho} \frac{\partial p_n}{\partial x} + \frac{\partial}{\partial x} \left[(v + \nu_t) \frac{\partial Hu}{\partial x} \right] \\ & + \frac{\partial}{\partial y} \left[(v + \nu_t) \frac{\partial Hu}{\partial y} \right] + \frac{1}{H} \frac{\partial}{\partial \sigma} \left[(v + \nu_t) \frac{1}{H} \frac{\partial Hu}{\partial \sigma} \right] \end{aligned} \quad (2)$$

$$\begin{aligned} & \frac{\partial Hv}{\partial t} + \frac{\partial Hvu}{\partial x} + \frac{\partial Hvv}{\partial y} + \frac{\partial Hv\tilde{w}}{\partial \sigma} \\ & = -gH \frac{\partial \eta}{\partial y} - \frac{H}{\rho} \frac{\partial p_n}{\partial y} + \frac{\partial}{\partial x} \left[(v + \nu_t) \frac{\partial Hv}{\partial x} \right] \\ & + \frac{\partial}{\partial y} \left[(v + \nu_t) \frac{\partial Hv}{\partial y} \right] + \frac{1}{H} \frac{\partial}{\partial \sigma} \left[(v + \nu_t) \frac{1}{H} \frac{\partial Hv}{\partial \sigma} \right] \end{aligned} \quad (3)$$

$$\begin{aligned} & \frac{\partial Hw}{\partial t} + \frac{\partial Hwu}{\partial x} + \frac{\partial Hwv}{\partial y} + \frac{\partial Hw\tilde{w}}{\partial \sigma} \\ & = -\frac{H}{\rho} \frac{\partial p_n}{\partial \sigma} + \frac{\partial}{\partial x} \left[(v + \nu_t) \frac{\partial Hw}{\partial x} \right] \\ & + \frac{\partial}{\partial y} \left[(v + \nu_t) \frac{\partial Hw}{\partial y} \right] + \frac{1}{H} \frac{\partial}{\partial \sigma} \left[(v + \nu_t) \frac{1}{H} \frac{\partial Hw}{\partial \sigma} \right] \end{aligned} \quad (4)$$

where $H = \eta + h$ is the total water depth, h is the still water depth below the datum, $\sigma = (z - \eta) / H$ is the new vertical coordinate, ρ is the water density, g is the gravitational acceleration, u , v and w are the velocity components in x , y , and z directions, respectively, ν is the molecular kinetic viscosity, ν_t is the eddy viscosity coefficient, and \tilde{w} is the vertical velocity in σ coordinate which can be calculated as:

$$\begin{aligned} \tilde{w} = & \frac{w}{H} - \frac{u}{H} \left(\sigma \frac{\partial H}{\partial x} + \frac{\partial \eta}{\partial x} \right) - \frac{v}{H} \left(\sigma \frac{\partial H}{\partial y} + \frac{\partial \eta}{\partial y} \right) \\ & - \frac{1}{H} \left(\sigma \frac{\partial H}{\partial t} + \frac{\partial \eta}{\partial t} \right) \end{aligned} \quad (5)$$

The eddy viscosity coefficient is calculated based on the Shear-Stress Transport (SST) $k - \omega$ model, where the transport equations for the turbulent kinetic energy k and the turbulence frequency ω are governed

by:

$$\frac{\partial k}{\partial t} + \frac{\partial(u_j k)}{\partial x_j} = \frac{\tau_{ij}}{\rho} \frac{\partial u_i}{\partial x_j} - \beta^* \omega k + \frac{\partial}{\partial x_j} \left[(v + \sigma_k v_i) \frac{\partial k}{\partial x_j} \right], \quad i, j = 1, 2, 3. \tag{6}$$

$$\frac{\partial \omega}{\partial t} + \frac{\partial(u_j \omega)}{\partial x_j} = \frac{\gamma}{v_i \rho} \tau_{ij} \frac{\partial u_i}{\partial x_j} + \frac{\partial}{\partial x_j} \left[(v + \sigma_\omega v_i) \frac{\partial \omega}{\partial x_j} \right] - \beta^* \omega^2 + 2(1 - F_1) \sigma_{\omega 2} \frac{1}{\omega} \frac{\partial k}{\partial x_j} \frac{\partial \omega}{\partial x_j}, \quad i, j = 1, 2, 3. \tag{7}$$

Then, v_i is calculated as:

$$v_i = \frac{\mu_i}{\rho} = \frac{k}{\omega} \tag{8}$$

where F_1 is a blending function, β^* , σ_k , γ , σ_ω and $\sigma_{\omega 2}$ are the SST model parameters taking their original values [24], τ_{ij} is the Reynolds stress evaluated using the Boussinesq relationship:

$$\tau_{ij} = \mu_t \left(\frac{\partial u_i}{\partial x_j} + \frac{\partial u_j}{\partial x_i} \right) - \frac{2}{3} \rho k \delta_{ij}, \quad i, j = 1, 2, 3. \tag{9}$$

The current model is solved with a two-step predictor-corrector scheme. The flow driven by the hydrostatic pressure is first calculated in the predictor step, and the flow field influenced by the non-hydrostatic pressure is updated in the corrector step. All the computations were conducted using an in-house code HydroFlow® [25].

1.2 Force Diagnostics

Considering a cylinder within the patch, which is labelled as number n , the force acting on this cylinder is defined by

$$\mathbf{F}_n = F_{xn} \vec{i} + F_{yn} \vec{j} \tag{10}$$

in which the streamwise component F_{xn} is referred to as the total drag force, and the lateral component F_{yn} is referred to the total lift force. The magnitude of F_{xn} and F_{yn} can be calculated by the shear stress and pressure acting on the cylindrical surface. After F_{xn} and F_{yn} are calculated, the drag and lift coefficients of the n th cylinder are obtained by

$$C_{dn} = \frac{F_{xn}}{0.5 \rho U^2 dH}, \quad C_{Ln} = \frac{F_{yn}}{0.5 \rho U^2 dH} \tag{11}$$

where d is the diameter of the cylinder and U is the depth-averaged velocity of the incoming flow [26]. The drag and lift coefficients of the whole patch are defined as

$$C_D = \frac{\sum_{n=1}^N F_{xn}}{0.5 \rho U^2 DH}, \quad C_L = \frac{\sum_{n=1}^N F_{yn}}{0.5 \rho U^2 DH} \tag{12}$$

in which D is the diameter of the patch and N is the number of cylinders in the patch.

1.3 Computational domain

The shallow water flows were simulated in a channel with a length of 11.52 m and a width of 1.2 m, which is illustrated in Fig. 1. At a distance of 3.0 m away from the inlet, a circular patch of cylinders with a staggered arrangement was placed. The patch’s diameter, D , is 0.22 m. The diameter of cylinders, d , was kept constant at 0.006 m. However, the number of emergent cylinders, N , varied from 48 to 252, which resulted in a wide range of the SVF from 0.03 to 0.15. The SVF was calculated using $SVF = \pi ad/4$, in which a (with units of m^{-1}) is frontal area per unit volume [8]. The distribution patterns of small cylinders inside the patches are shown in Fig. 2.

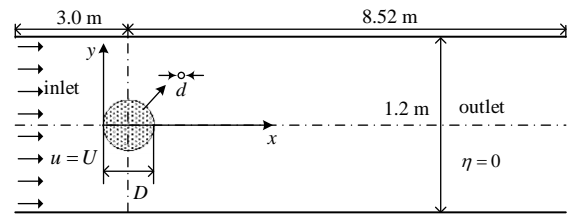


Fig. 1 Top view of the computational domain.

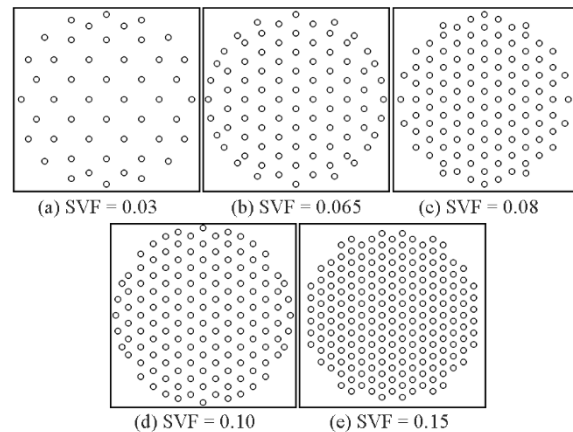


Fig. 2 Distribution of small cylinders inside the patch.

1.4 Study cases and numerical implementation

The slip solid wall boundary condition was imposed at both sidewalls of the channel. To be able

to resolve the detailed flow structures around individual cylinders, the no-slip wall boundary condition with a fine resolution at the cylindrical surface is necessary. Hence, a minimum normal length of 0.1 mm was specified to maintain a dimensionless wall distance of approximately 1 ~ 2, i.e. $\Delta^+ = 1 \sim 2$ (see Fig. 3(a)). At the bottom, the standard wall functions were applied, and the nearest nodes above the bed were adjusted to satisfy the log-law condition, i.e. $z^+ > 11.63$. The current spatial discretization consisted of unstructured meshes (see Fig. 3(b)) in the horizontal direction and multi-layers in the vertical direction.

$$\frac{u}{u^\tau} = \frac{1}{\kappa} \ln(Ez^+) \quad k = \frac{(u^\tau)^2}{\sqrt{C_\mu}} \quad \omega = \sqrt{C_\mu} \frac{u^\tau}{\kappa z} \quad (13)$$

In the above wall functions, Von Karman’s constant $\kappa = 0.41$, wall roughness parameter $E = 9.8$ for smooth walls, $C_\mu = 0.09$ is an empirical coefficient, u^τ is the friction velocity, z^+ is a dimensionless distance from the wall $z^+ = zu^\tau / \nu$.

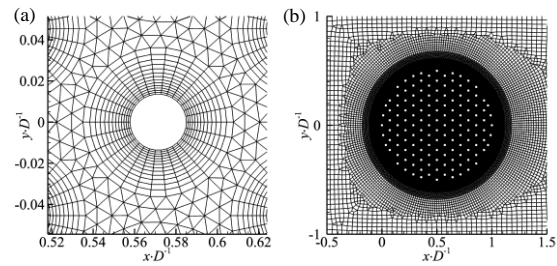


Fig. 3 Computational mesh: (a) close-up mesh around a single cylinder, (b) mesh around the patch.

To model a uniform and steady open channel flow, a steady flow discharge was specified at the inlet, and the water depth was fixed at the outlet. The time step was 0.0005 s throughout the simulations. The computations proceeded until the flow was statistically stationary. Then, the flow variables at all grids were recorded at a frequency of 20 Hz for a time period of 60 s.

Table 1 Configurations and flow statistics of studied cases.

Case	SVF	H(m)	C_f	S	U_{1s}/U	U_{1e}/U	U_2/U	L_1/D	C_D	St_D
P1H1	0.03	0.133	0.00502	0.008	0.55	0.55	1.10	7.73	0.93	0.26
P1H2	0.03	0.100	0.00531	0.012	0.55	0.55	1.10	7.30	0.93	0.26
P1H3	0.03	0.067	0.00606	0.020	0.55	—	1.10	—	0.89	0.24
P1H4	0.03	0.04	0.00682	0.038	0.55	—	1.10	—	0.96	0.33
P1H5	0.03	0.03	0.00771	0.057	0.55	—	1.10	—	1.01	0.32
P2H1	0.065	0.133	0.00502	0.008	0.25	0.086	1.22	4.17	1.26	0.18
P2H2	0.065	0.100	0.00531	0.012	0.25	0.098	1.22	5.17	1.27	0.19
P2H3	0.065	0.067	0.00606	0.020	0.25	0.153	1.22	5.77	1.23	0.19
P2H4	0.065	0.04	0.00682	0.038	0.25	0.247	1.22	5.84	1.31	0.21
P2H5	0.065	0.03	0.00771	0.057	0.25	—	1.22	—	1.35	0.22
P3H1	0.08	0.133	0.00502	0.008	0.20	0.0	1.24	3.82	1.38	0.15
P3H2	0.08	0.100	0.00531	0.012	0.20	0.002	1.24	4.11	1.38	0.16
P3H3	0.08	0.067	0.00606	0.020	0.20	0.030	1.24	5.17	1.38	0.17
P3H4	0.08	0.04	0.00682	0.038	0.20	0.14	1.24	4.87	1.40	0.19
P3H5	0.08	0.03	0.00771	0.057	0.20	0.20	1.24	4.87	1.47	0.22
P4H1	0.10	0.133	0.00502	0.008	0.14	-0.032	1.26	2.91	1.45	0.16
P4H2	0.10	0.100	0.00531	0.012	0.14	-0.020	1.26	3.51	1.47	0.16
P4H3	0.10	0.067	0.00606	0.020	0.14	-0.021	1.26	4.57	1.45	0.16
P4H4	0.10	0.04	0.00682	0.038	0.14	-0.063	1.26	4.97	1.48	0.19
P4H5	0.10	0.03	0.00771	0.057	0.14	0.122	1.26	5.17	1.56	0.21
P5H1	0.15	0.133	0.00502	0.008	0.02	-0.14	1.27	1.55	1.35	0.17
P5H2	0.15	0.100	0.00531	0.012	0.02	-0.14	1.27	1.56	1.37	0.18
P5H3	0.15	0.067	0.00606	0.020	0.02	-0.15	1.27	1.71	1.34	0.18
P5H4	0.15	0.04	0.00682	0.038	0.02	-0.11	1.27	2.31	1.34	0.19
P5H5	0.15	0.03	0.00771	0.057	0.02	-0.014	1.27	3.36	1.40	0.19
SH1	1.0	0.133	0.00502	0.008	—	-0.28	1.28	—	0.92	0.15
SH2	1.0	0.100	0.00531	0.012	—	-0.21	1.28	—	0.98	0.15
SH3	1.0	0.067	0.00606	0.020	—	-0.19	1.28	—	1.04	0.14
SH4	1.0	0.04	0.00682	0.038	—	-0.29	1.28	—	1.09	0.18
SH5	1.0	0.03	0.00771	0.057	—	-0.17	1.28	—	1.43	0.18

All the simulations were conducted with patch Reynold number $Re_D = UD/\nu = 21560$. The

simulations were carried out with SVF = 0.03, 0.065, 0.08, 0.10 and 0.15, and the water depth $H = 0.133$ m,

0.10 m, 0.067 m, 0.04 m and 0.03 m in different runs. Additional simulations of the flow around a solid cylinder as large as the whole patch (SVF = 1.0) were also conducted for comparison. A summary of the simulated cases were listed in Table 1, in which “P1”, “P2”, “P3”, “P4”, “P5” and “S” refer to the different patch densities, and “H1”, “H2”, “H3”, “H4” and “H5” refer to different water depths. For brevity, the notations of simulation cases, given in the first column of the table, will be used in the following part of this paper. Important flow characteristics were also listed in the table, which will be explained later. The bed friction coefficient was calculated using $C_f = 2\tau/\rho U^2$, in which τ is the bed shear stress obtained from simulations of flow without the vegetation patch. $S = C_f D/H$ is the shallow wake stability parameter. Behind the patch, a steady wake exists, within which the velocity is denoted by U_1 . Chang & Constantinescu [15] showed that the streamwise velocity decreased along the steady wake when $SVF > 0.05$, and they defined U_1 as the velocity exiting the patch. In this study, two velocity scales are defined to gain a more detailed description: U_{1s} at the starting point of the steady wake, which is equal to the velocity exiting the patch, and U_{1e} at the end of the steady wake. To eliminate the effect of cylinder-scale wake, U_{1s} is obtained by the mean streamwise velocity at position $x = 1.1D$, $y = 0$. The magnitude of L_1 was measured from the end of the patch to the point where the mean streamwise velocity \bar{u} began to increase, i.e. $d\bar{u}/dx = 0$. As an example, Fig. 4 illustrates the positions of U_{1s} , U_{1e} and L_1 . It is noticed that the measurements of L_1 get invalid when $U_{1e} \geq U_{1s}$. U_2 is the velocity at the outer edge of the SSLs. Instantaneous records of the lateral velocity, v , were used to identify the patch-scale vortex shedding frequency (f_D), using the fast Fourier transform method (FFT), from which the Strouhal number, $St_D = f_D D/U_2$, was calculated.

2. Results and analysis

2.1 Model verification

The numerical model was firstly verified against the measurements by Zong & Nepf [12]. The mean velocity profiles \bar{u} (at $y = 0$) and \bar{v} (at $y = D/2$) in the longitudinal direction of cases P1H1 and P4H1 were plotted in Fig. 4. The vertical solid line and dashed line represent the upstream end and downstream end of the patch, respectively. The good agreements between the modeled and measured velocities suggest that the present model is accurate.

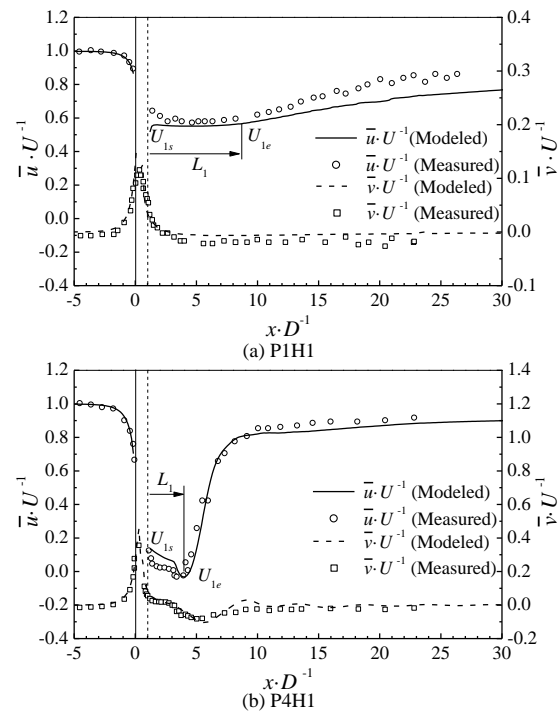


Fig. 4 Verifications of the computed mean velocities.

2.2 Mean flow and turbulent structure

2.2.1 Longitudinal distribution of velocity

With the presence of an impervious obstruction in an open channel, water is forced to flow around it only. In contrast, a porous obstruction can divide the incoming flow into two parts. One part flows directly through the obstruction, which is often referred to as bleed flow, while the other part wraps around it. The obstruction causes the decrease of \bar{u} on the immediate upstream side and in the wake, which was shown in Fig. 5. For all the patches (P1-P5) in Fig. 5, the flow diversion, i.e. change of the incoming flow, began at approximately D upstream of the patch, consistent with the arguments of Rominger & Nepf [27]. The streamwise velocity \bar{u} at the leading edge of the patch was found to be dependent on SVF only. The flow through the patch encountered solid cylinders inside the patch, then \bar{u} decreased dramatically due to the drag. As the stem density of the patch increased, the summation of the drag force would increase, and the velocity exiting the patch, U_{1s} , decreased monotonously (see Fig. 5(a-e)). This relationship between U_{1s} and SVF was also confirmed by Chen, et al. [14]. The lower limit of U_{1s} was found to be zero for a dense patch [12], which was also confirmed in Fig. 5(e). Specifically, for a patch with sufficiently large SVF, e.g. $SVF = 0.15$ in this study, the bleed flow entering the patch decelerated so rapidly by a large number of cylinders that only a small amount of water can get to the downstream end of the patch. The streamwise velocity \bar{u} behind a solid body (Fig. 5(f))

was negative because of the flow recirculation occurred immediately behind the body. In addition, the magnitude of U_{1s} was found to be independent on the water depth H for all patches. Unlike U_{1s} , U_{1e} exhibited a significant dependence on the water depth. U_{1e} at small water depths (H3-H5) was larger than that

at large water depths (H1-H2), and it increased with the decrease of H . Particularly, \bar{u} became larger than U_{1s} for sparse patches (P1H4 and P1H5 in Fig. 5(a) and P2H5 in Fig. 5(b)), which resulted in $U_{1e} = U_{1s}$.

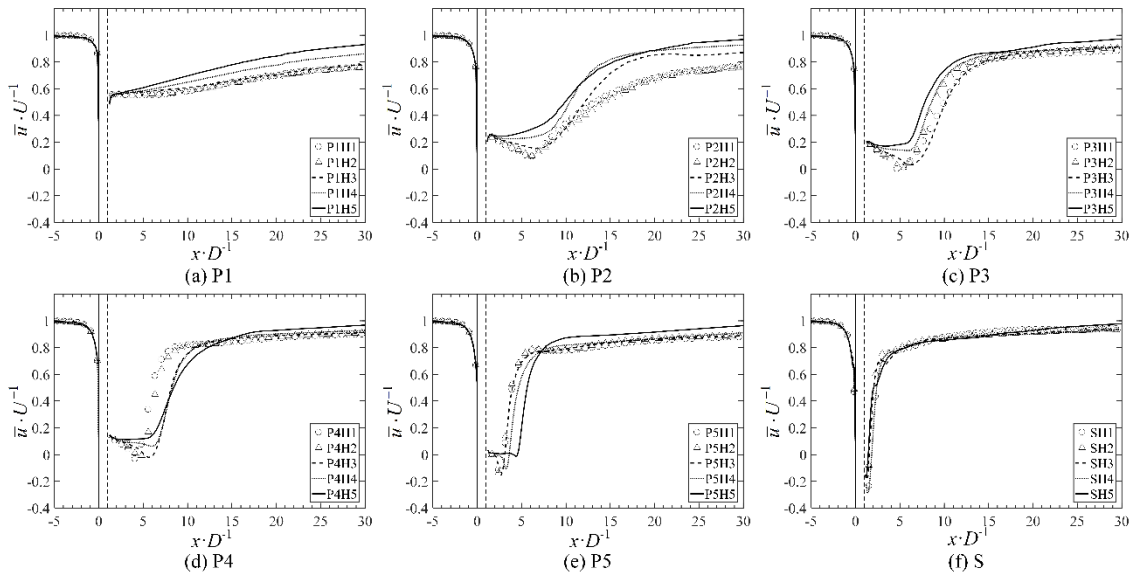


Fig. 5 Longitudinal distributions of velocity along the centreline.

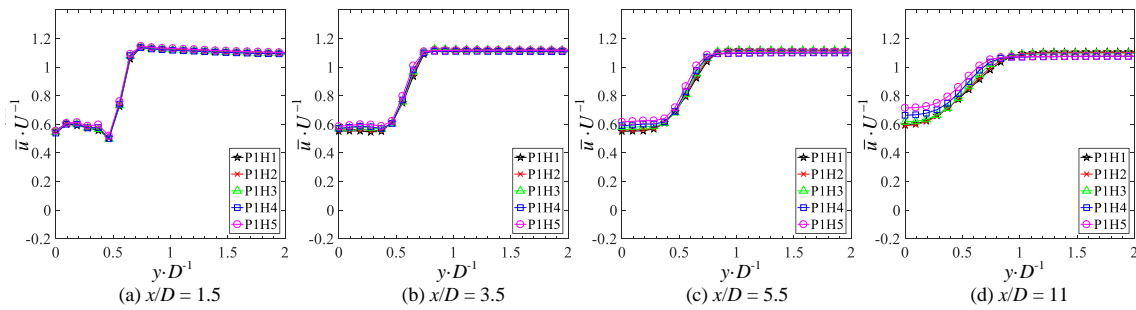


Fig. 6 (Color online) Lateral profiles of velocity for patch P1 (SVF = 0.03).

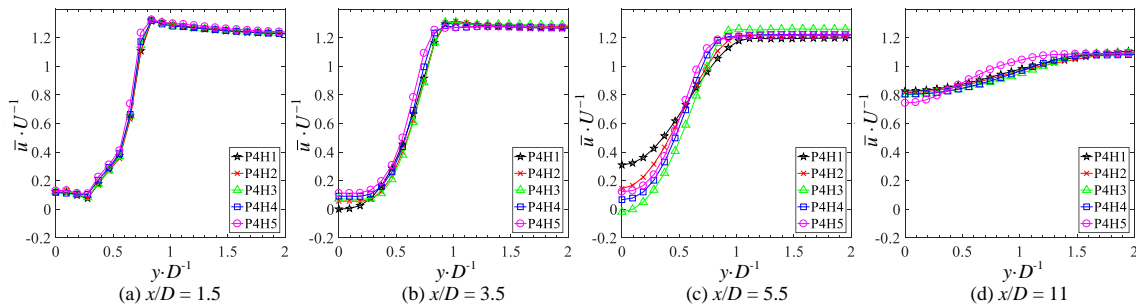


Fig. 7 (Color online) Lateral profiles of velocity for patch P1 (SVF = 0.10).

2.2.2 Lateral distribution of velocity

The lateral profiles of mean streamwise velocity

were plotted in Fig. 6 and Fig. 7 to reveal the lateral structure of wake and its evolution downstream. In the

steady wake, separated shear layers (SSLs) were formed along the two sides of the wake region. The velocity deficit in the steady wake enhanced the development of SSLs, and the development did not cease until these SSLs met at the centerline of the wake. Since the position where the SSLs meet is at the end of the steady wake, the mean streamwise velocity at this position should just be equal to U_{1e} .

For a sparse patch P1 (SVF=0.03), the mean velocity cross the steady wake was almost uniform along the lateral direction immediately downstream the patch (Fig. 6(a)) regardless of the water depth. Further downstream the patch (Fig. 6(b-c)), the SSLs began to grow, resulting in the wake narrowing. Fig. 6 also revealed a constant velocity outside the wake (U_2 at approximately $y/D > 0.75$). The velocity \bar{u} of flow between the SSLs and the wake was always between U_{1e} and U_2 . The SSLs met at $x/D \approx 9$ (from Fig. 6 and Table 1), where the steady wake region

ended. Behind the steady wake (Fig. 6(d)), \bar{u} began to recover and slowly approached the free stream velocity (U). The recovery was observed to be faster at smaller water depths (H4 and H5). Surprisingly, the dense patch exhibited a different wake structure as shown in Fig. 7 because of the presence of von-Karman vortex street. Firstly, the steady wake velocity U_{1s} was much lower than that of the sparse patch (Fig. 7(a-b)). Secondly, the growth of the steady wake was faster. The SSLs met at $x/D < 5.5$, and a negative velocity was found in Fig. 7(c). Lastly, the recovery of velocity behind the steady wake also became faster, mostly due to the enhanced transverse mixing as a result of the patch-scale vortices. The influence of water depth was obviously captured in Fig. 7(b-c). At $x/D = 5.5$, the velocity recovery had already started for P4H1, while it just began for P4H5 causing an elongated steady wake.

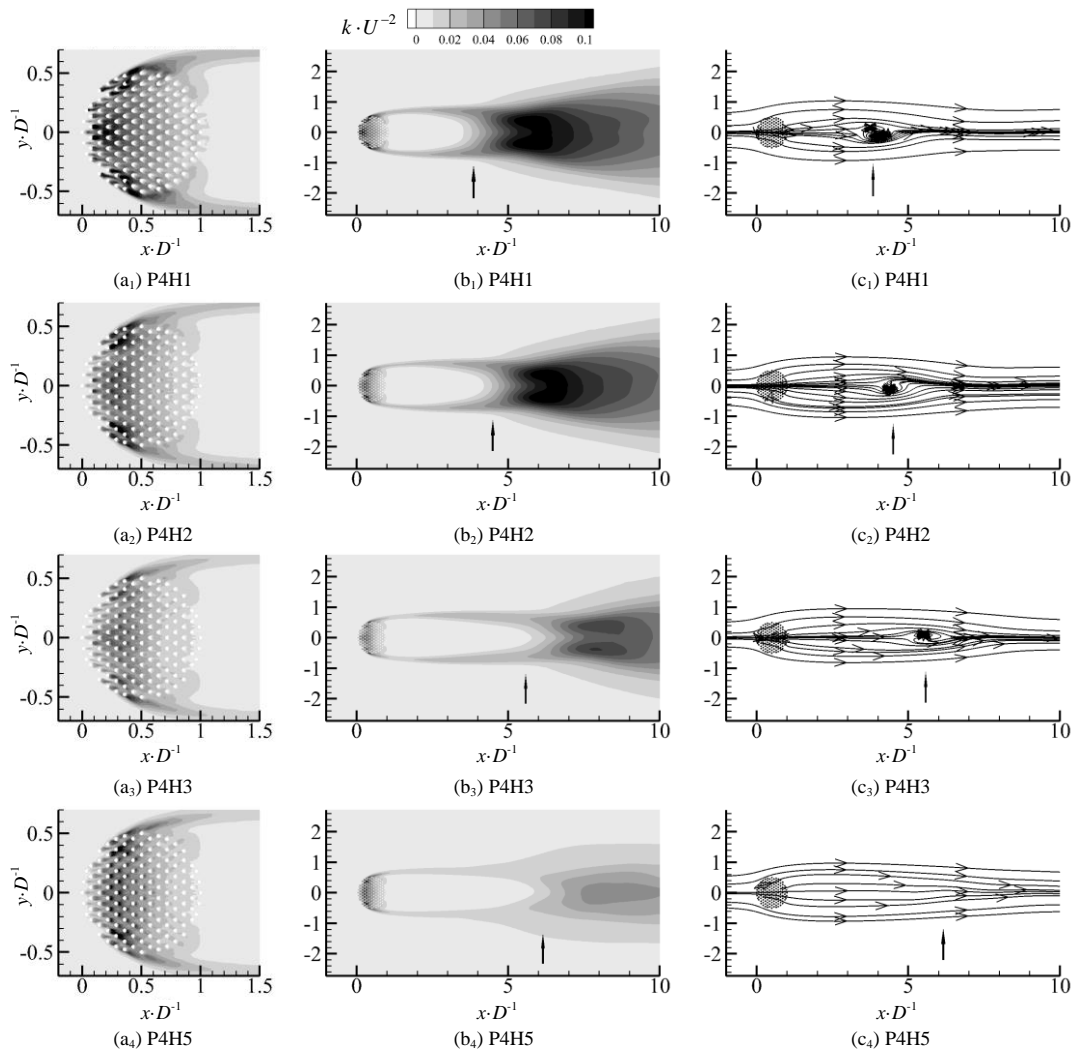


Fig. 8 Mean flow and turbulence structure of patch P1: (a) TKE within the patch; (b) TKE outside the patch; (c) Streamlines of the mean flow.

2.2.3 Turbulence structure

Knowledge of the distribution of turbulent kinetic energy (TKE) within and outside the patch is of particular importance in cases where the cylinders are natural stems. The presence of high TKE regions behind the patch has a direct effect on nutrient availability and sediment transport [15]. Both cylinder-scale and patch-scale turbulence are generated in water flows through a patch of cylinders. For a sparse patch (SVF = 0.03) as shown in Fig. 8, an elevated turbulence level was apparent within the patch (Fig. 8(a₁)). Because the gap distance between cylinders was much larger than the cylinder diameter (d), the interactions between cylinders were weak, and the wake vortices were shed from most of the cylinders. As a comparison, TKE in the wake behind the patch was relatively weak (Fig. 8(b₁)), suggesting that the patch-scale turbulence was not strong. The

streamlines of mean flow were very straight as illustrated in Fig. 8(c₁-c₄), indicating that the strength of the bleed flow was high, and the lateral momentum exchange was weak. As a result, not much turbulence was generated in the wake of the patch. The TKE inside the patch decreased with the water depth from H1 to H5, and this could be mainly attributed to the strong bed friction. The wake stability parameter for cylinders, $S = C_f d/H$, is much smaller than the critical value 0.2, so the cylinder-scale vortices still existed at low water depths. Although turbulence was weakened in the patch, it was still stronger than that in the steady wake. This agreed with the observations of Nepf, et al. [28], suggesting that turbulence within the patch was dominated by cylinder-scale eddies. The bed friction also resulted in an attenuation of turbulence in the SSLs (Fig. 8(b₁-b₄)), which led to the reduction of velocity deficit between U_{1e} and U_2 .

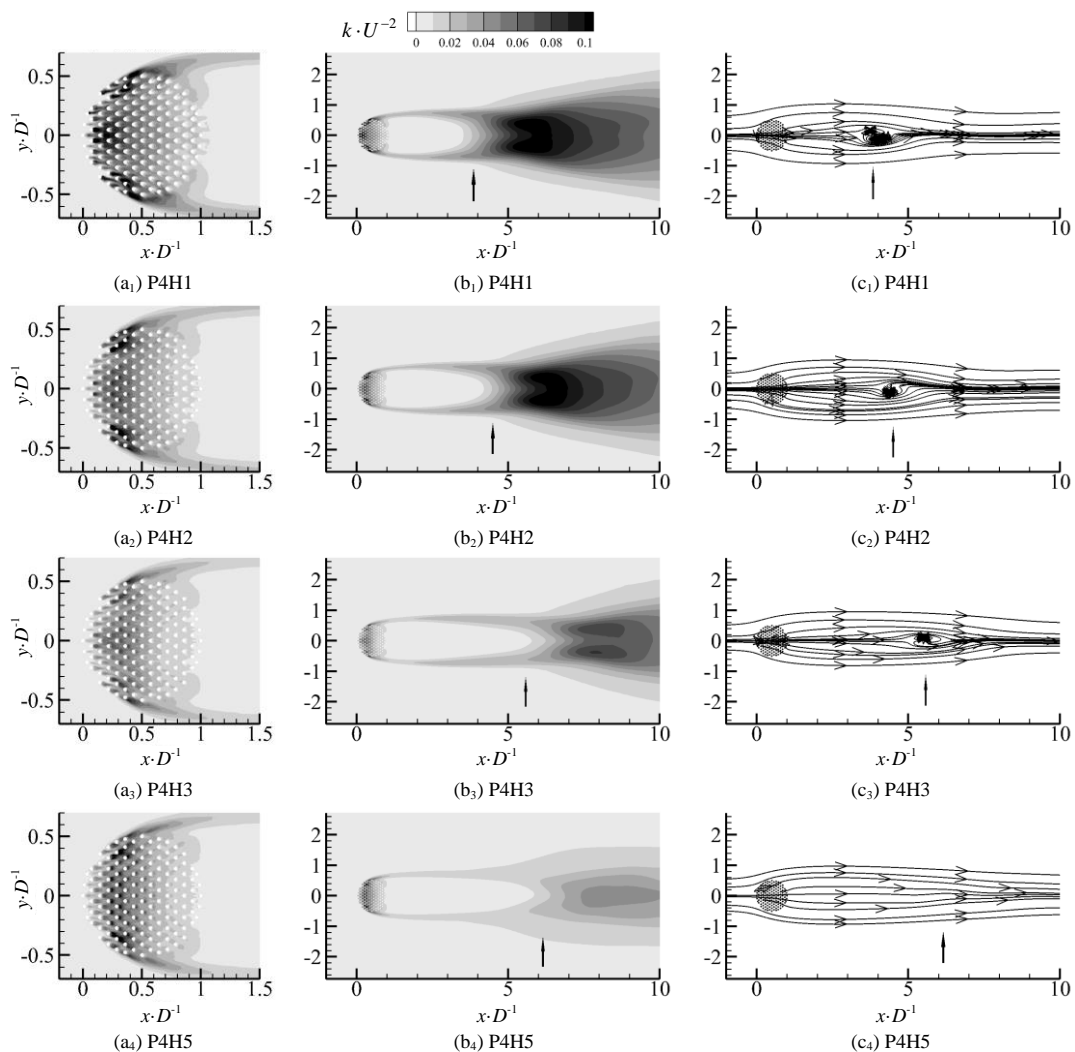


Fig. 9 Mean flow and turbulence structure of patch P4: (a) TKE within the patch; (b) TKE outside the patch; (c) Streamlines of the mean flow.

When considering a patch of medium density ($SVF = 0.10$), the shear layers of upstream cylinders extended to the downstream cylinders inside the patch, which then impeded the shedding of vortices from downstream cylinders [29, 30]. Therefore, the high TKE region was only observed adjacent to the upstream half of the cylinders (Fig. 9(a)). The bleed flow decreased significantly due to the high drag of upstream cylinders, so most water flowed around the patch instead of going through it. This strong flow diversion was demonstrated in Fig. 9(c) by the distorted streamlines. Similar to the case of a sparse patch, the steady wake region has a low TKE level. The largest amplification of TKE occurred at some distance behind the steady wake. At the end of the steady wake, the SSLs interacted with each other, which resulted in the formation of billow vortices. As is known that a recirculation zone appears immediately behind a solid body at certain Reynolds

numbers [15], the recirculation zone behind a dense patch was more elongated compared to the solid body. The position where the recirculation bubble formed was close to the end of the steady wake, which was indicated by an upward black arrow in Fig. 9(b-c). The advection of patch-scale oscillating vortices was mainly responsible for the amplification of TKE. Nevertheless, the patch-scale vortices were susceptible to bed friction. As is shown in Fig. 9(b₁-b₄), TKE decreased monotonously with the decrease of H , and the steady wake extended further downstream as H decreased. At a very low water depth H_5 (Fig. 9(c₄)), the recirculation bubble eventually disappeared, which indicated that the interaction between the two SSLs was inhibited by bed friction. Although the bed friction was strong, TKE in the far wake of a dense patch was still noticeable (Fig. 9(b₄)).

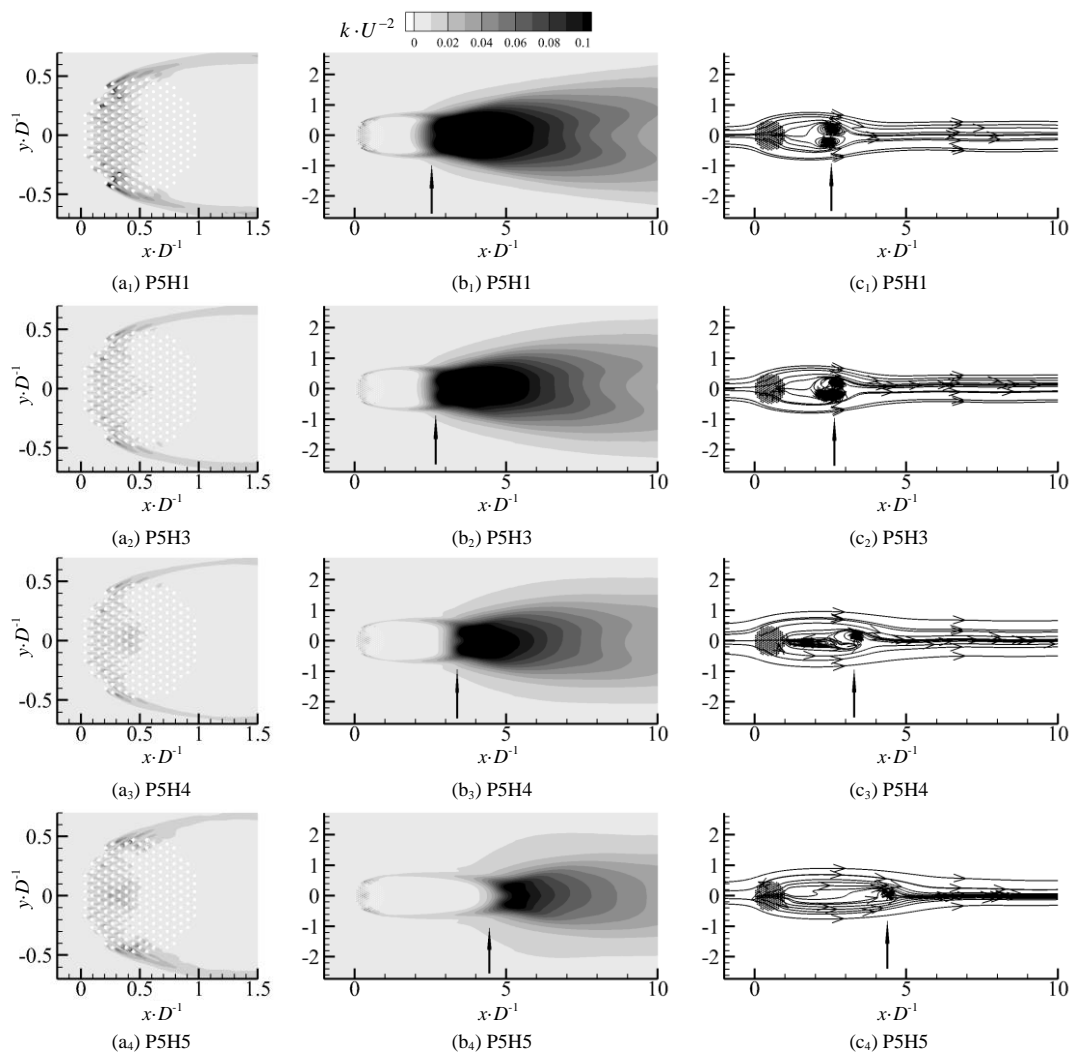


Fig. 10 Mean flow and turbulence structure of patch P5: (a) TKE within the patch; (b) TKE outside the patch; (c) Streamlines of the mean flow.

For a patch of high density ($SVF = 0.15$), the wakes of the upstream solid cylinders were significantly interfered by the downstream cylinders. The narrow gaps between cylinders suppressed the formation of the cylinder-scale vortices, which contributed to a low TKE region in the patch. The low TKE region occupied nearly the whole patch, excluding only a few cylinders near the lateral edges of the patch (Fig. 10(a)). These cylinders at the edge were located in the region where SSLs formed, and the restriction from neighboring cylinders was not so strong. As opposed to the patch with $SVF = 0.10$, the steady wake was shortened (Fig. 10(b)). Because it comprised of a larger number of cylinders, the wake pattern of a highly dense patch showed a trend similar

to that of a solid body. Recirculation bubble was formed closer to the patch, but there was still some distance to the end of the patch (Fig. 10(c)). The peak TKE occurred in the region behind the steady wake, where the patch-scale vortices formed. A smaller water depth resulted in a lower level of patch-scale turbulence (Fig. 10(b₁-b₄)). The steady wake length, as well as the distance between the recirculation bubble and the patch, increased monotonously as H decreased. As the patch-scale turbulence was more intense than the patch with $SVF = 0.10$, the formation of the recirculation bubble was not completely inhibited by bed friction in this case (Fig. 10(c₄)).

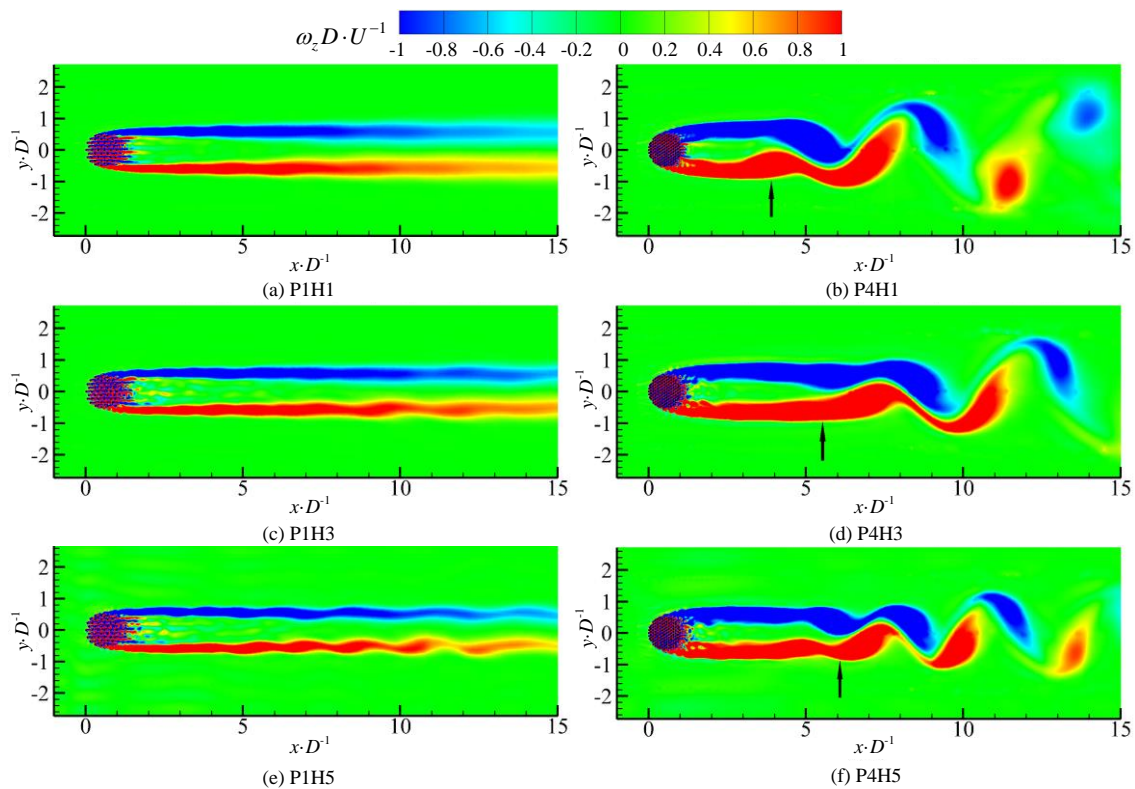


Fig. 11 (Color online) Instantaneous vertical vorticity. The solid arrows indicate the end of steady wake.

2.3 Instantaneous vortical structures

The wake structure behind the patch was further investigated by the instantaneous vertical vorticity contours as shown in Fig. 11. Both SSLs were visualized at the shoulders of the patch, regardless of the SVF. For a dense patch, the velocity deficit between the SSLs and the steady wake was higher than the case of a sparse patch, which caused higher shear stress in SSLs. This is why the intensity of the vertical vorticity in Fig. 11(b) was stronger than that in Fig. 11(a). When the SSLs merged at the end of the

steady wake, the shear instability might occur, depending on the relative importance of the velocity deficit and the bed friction. If the velocity deficit was large enough and the bed friction was insignificant, the wake became unstable and the patch-scale vortex street was formed. The appearance of the patch-scale vortex street was a signature to distinguish the wake pattern of a dense patch from a sparse patch (Fig. 11(b, d, f)). As discussed in section 2.2, the bed friction imposed a negative effect on the development of the patch-scale turbulence. Therefore, the vorticity level

behind the sparse patch was weaker when the water depth was shallow (Fig. 11(a, c, e)). Despite the large bed friction, the vortex street behind a dense patch was still identified at a small water depth (Fig. 11(f)), although the onset point was delayed further downstream compared with those cases shown in Fig.

11(b) and Fig. 11(d). The bed friction dissipated flow energy and suppressed the spatial evolution of the SSLs behind a dense patch. As a result, the SSLs became narrower in Fig. 11(f).

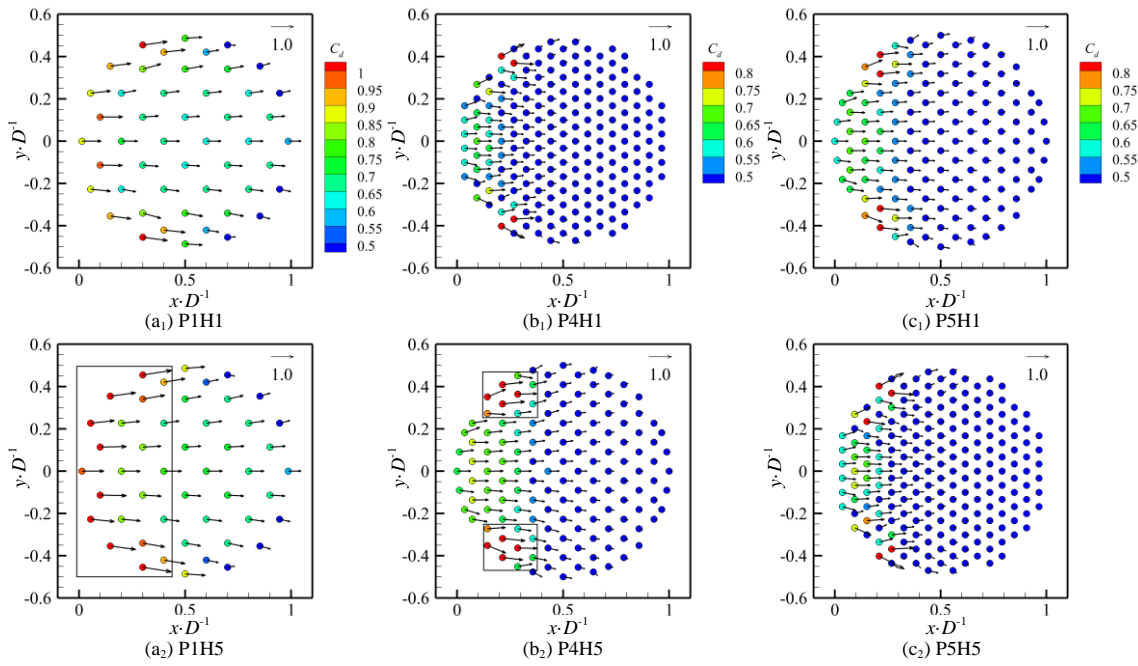


Fig. 12 (Color online) Mean non-dimensional forces acting on cylinders.

2.4 Non-dimensional forces on individual cylinders

Fig. 12 shows the flow-induced forces acting on individual cylinders for three example patches, P1, P4 and P5, which represent a sparse patch, a medium dense patch and a high dense patch, respectively. Every cylinder is visualized as a small circle and the drag coefficient distribution is shown using colored legends. The arrow radiating from the center of each cylinder indicate the magnitude and the mean direction of the resultant forces. At low SVF (Fig. 12(a₁)), the maximum C_{dn} was not observed on the most upstream cylinders, but on cylinders a few rows behind the most upstream cylinders^[31]. These cylinders were located in the wake of the most upstream cylinders and experienced an accelerated bleed, which resulted in larger drag forces. However, the bleed flows became weaker at a large SVF, and thus the largest drag forces did not exert on the cylinders behind the front cylinders (Fig. 12(b₁-c₁)). Instead, the cylinders in the vicinity of the shoulders of the patch, approximately at $y/D = \pm 0.4$, were exposed to the accelerated diverged flow. Most of the flow was around the patch instead of through it, leading to increased drag forces on these cylinders. For a high dense patch (P5 in Fig. 12(c₁)), the

maximum C_{dn} took place on the cylinders at the same location as patch P4. The total force on the front cylinders had a lateral component, indicating that the flow diversion occurred. Due to the significant blocking effect, the position of flow diversion approached the front cylinders, and the number of cylinders experienced high drag force reduced. The forces on cylinders at low water depth H5 are shown in Fig. 12(a₂-c₂). An amplification of drag forces was found within each patch. For patch P1, the cylinder-scale wakes did not interact with one another because of the large gap between cylinders. As a result, almost all of the cylinders were affected, especially the front cylinders (marked by a black rectangle in Fig. 12(a₂)). For dense patches P4 and P5, the most susceptible cylinders were located at the front of the patch and the regions where flow diverged (marked by two black squares in Fig. 12(b₂)). These cylinders in the rectangle and squares were exposed to either the diverged flow or the bleed flow.

Fig. 12 revealed larger drag forces on individual cylinders of the patch when the water depth gets shallower. To investigate the influence of these increased drag forces as a whole patch, the time-averaged total drag coefficient is depicted in Fig. 13. The flow condition is parameterized by the

stability parameter S . A monotonically increasing relationship was found between C_D and SVF when $SVF < 0.10$. As SVF increased to 0.15, the patch behaved like a solid body in flows, the drag forces acting on the downstream cylinders in the patch were negligibly small (Fig. 12(c₂)), which resulted in a decrease of C_D . The amplification of drag forces on individual cylinders contributed to the increasing of C_D when $S > 0.02$, but the increment was very subtle. The maximum relative growth rate was only 5.3%, calculated from case P4H4 to P4H5. This is the reason why no significant differences in U_{1s} were found among different water depths [14].

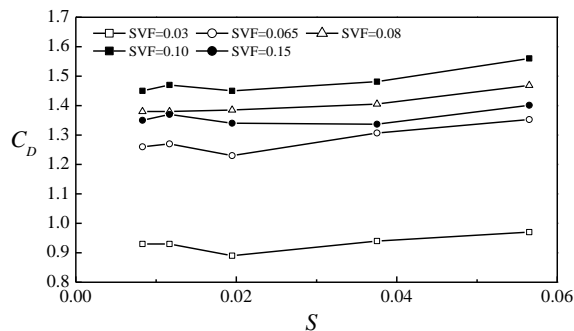


Fig. 13 Time-averaged total drag coefficient of the patches.

2.5 Velocity and length scale of the steady wake

The mean streamwise velocity at the starting point of the steady wake, U_{1s} , was found to be independent on the bed friction, but associated with the interior velocity inside the patch. The interior velocity was mainly driven by turbulent stress at low flow blockage ($C_D a D < 4$), but it was dominated by pressure gradient when $C_D a D \geq 4$. The flow resistance force increased with the patch drag, which was large enough to make bed friction negligible within the patch [27]. However, the streamwise velocity at the end of the steady wake, U_{1e} , and the spatial extent of the wake were affected significantly by bed friction (Fig. 14). U_{1e} decreased monotonously as SVF increased (Fig. 14(a)), which was attributed to the large patch drag. The negative value of U_{1e} for $SVF = 0.10$ and $SVF = 0.15$ indicated the presence of recirculation bubbles. The magnitude of U_{1e} appeared to be constant when $S < 0.02$, but increased with S when S exceeded 0.02. When S increased, U_{1e} gradually increased to U_{1s} . As the streamwise velocity in the steady wake increased, the velocity difference between the steady wake and the SSLs decreased. As a consequence, the intensity of the shear in the SSLs weakened, and the steady wake extended further (Fig. 14(b)). Because U_{1e} was equal to U_{1s} for $SVF = 0.03$, a tiny drop of L_1 was observed, which was within the uncertainty of measurement. Similar to the change of U_{1e} , there was a maximum value for L_1 , which

appeared when U_{1e} reached its upper limit U_{1s} . The value of S , for which the maximum L_1 appeared was related to SVF, and it was higher for large SVF than small SVF.

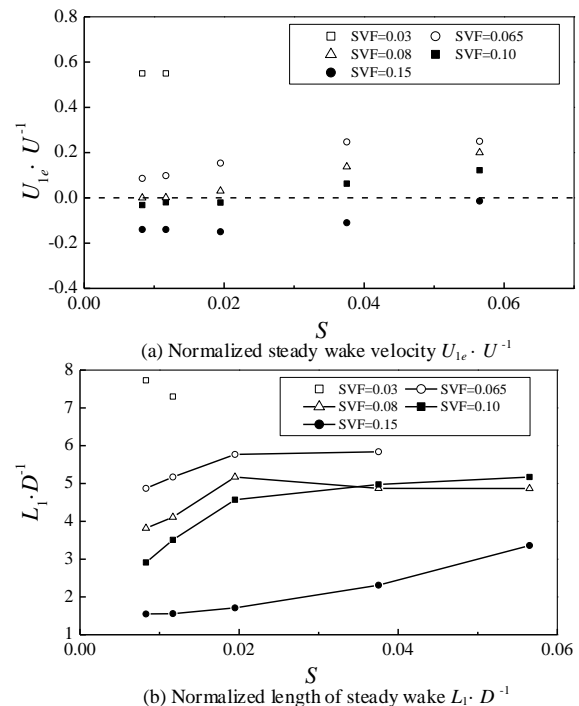


Fig. 14 Dependence of U_{1e} and L_1 on S .

2.6 Strouhal number

Behind the steady wake, an unsteady wake exists. Variations of the instantaneous lateral velocity, v , with time were plotted to study the unsteady wake oscillations (Fig. 15(a)). Then, the Strouhal number, St_D , can be obtained by the FFT spectral analysis (Fig. 15(b)). It is noted that bed friction may suppress the formation of von Karman vortex street. Chen & Jirka [32] studied the critical shallow water conditions, characterized by stability parameter S . To investigate the influence of bed friction (S) on wake oscillations, the Strouhal number is plotted in Fig. 16. For cases without a visual vortex street ($SVF = 0.03$), the St_D was still calculated as the small wake instability was present. The St_D for a dense patch ($SVF > 0.03$) at small S was around 0.17, which was consistent with the measurements of Zong & Nepf [12]. As S increased, St_D also increased, indicating that suppression of bed friction became substantial. It can be noticed that the dependence of St_D on S in Fig. 16 and the dependence of U_{1e} on S in Fig. 14(a) share some common characteristics in some sense. This is because that the endpoint of the steady wake is also the start point of the unsteady wake. As S increased, U_{1e} increased due to strong bed friction. The increase of U_{1e} reduced the lateral velocity difference between the flows inside

and outside the wake, which impeded the occurrence of shear instability. As a result, the formation of vortex street was suppressed, which resulted in an increase of St_D . However, the bed friction was not strong enough to inhibit the formation of vortex street. The maximum Strouhal number of a dense patch was smaller than 0.23, while Chen & Jirka [32] found that the vortex street disappeared in cylinder wakes when $St_D > 0.23$.

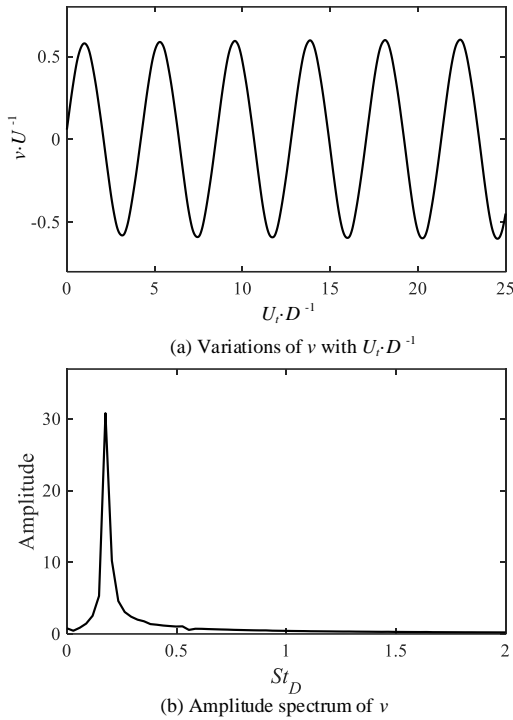


Fig. 15 Variations and amplitude spectrum of the lateral velocity, v , at $x/D=3.0$, $y/D=0$ for case P5H1.

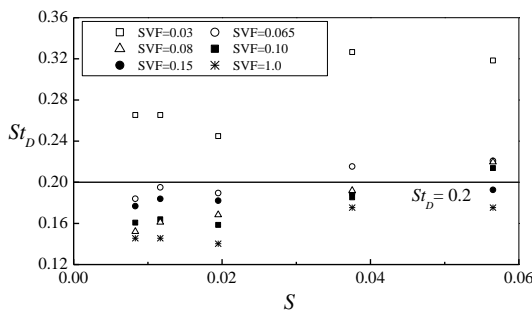


Fig. 16 Strouhal number St_D versus S .

3. Discussions

3.1 Formalizing the bed friction influence

To understand the dynamic relationship between steady wake and bed friction, the shallow water equations in conservative form are considered. With

bottom friction and hydrostatic pressure assumption, the mass conservation and streamwise momentum conservation equations read:

$$\frac{\partial H}{\partial t} + \frac{\partial(H\bar{u})}{\partial x} + \frac{\partial(H\bar{v})}{\partial y} = 0 \tag{14}$$

$$\frac{\partial(H\bar{u})}{\partial t} + \frac{\partial(H\bar{u}\bar{u})}{\partial x} + \frac{\partial(H\bar{u}\bar{v})}{\partial y} = -\frac{\partial}{\partial x}\left(\frac{gH^2}{2}\right) - \frac{C_f}{2}\bar{u}\sqrt{\bar{u}^2 + \bar{v}^2} + \frac{1}{\rho}\left[\frac{\partial}{\partial x}(H\bar{\tau}_{xx}) + \frac{\partial}{\partial y}(H\bar{\tau}_{xy})\right] \tag{15}$$

Here, τ is the shear stress. The overbar denotes the average over water depth. Within the steady wake, the flow variables H , \bar{u} and \bar{v} do not change much with time. For large enough Reynolds numbers, the molecular viscous term is neglected [33]. The lateral divergence of turbulent stress at the centreline ($y/D = 0$) is small and negligible [27, 12]. With these assumptions and using Reynolds averaged equations, the equations for continuity and streamwise momentum in steady wake can be simplified as:

$$\frac{\partial(H\bar{u})}{\partial x} + \frac{\partial(H\bar{v})}{\partial y} = 0 \tag{16}$$

$$\bar{u}\frac{\partial\bar{u}}{\partial x} + \bar{v}\frac{\partial\bar{u}}{\partial y} = -g\frac{\partial H}{\partial x} - \frac{C_f}{2H}\bar{u}\sqrt{\bar{u}^2 + \bar{v}^2} \tag{17}$$

For brevity, the symbol of time-averaging is omitted. To find the relationship between U_{1s} , U_{1e} and L_1 , the streamwise momentum Eq. (17) is scaled using the following characteristic values:

$$\begin{aligned} x &\sim L_1, \quad y \sim \frac{D}{2}, \quad \bar{u} \sim U_{1s}, \\ \bar{v} &\sim \frac{DU_{1s}}{2L_1}, \quad \frac{\partial\bar{u}}{\partial x} \sim \frac{U_{1e}-U_{1s}}{L_1}, \quad H \sim H_\infty. \end{aligned} \tag{18}$$

H_∞ is the water depth of free stream. The final non-dimensional equations are then

$$\frac{U_{1s}(U_{1e}-U_{1s})}{L_1} \sim -\frac{C_f}{2H_\infty}U_{1s}^2\sqrt{1+\left(\frac{D}{2L_1}\right)^2} - g\frac{\partial H}{\partial x} \tag{19}$$

To relate U_{1s} and U_{1e} with L_1 , a new dimensionless parameter, r , is defined, which characterises the development rate of streamwise velocity in the steady wake. Multiplying Eq. (19) by $2D/U^2$, the relationship can be adopted in terms of r and S :

$$r = \frac{(U_{1e} - U_{1s})D}{UL_1} \quad (20)$$

$$\frac{2U_{1s}}{U} r \sim -\left(\frac{U_{1s}}{U}\right)^2 \sqrt{1 + \left(\frac{D}{2L_1}\right)^2} S - \frac{2gD}{U^2} \frac{\partial H}{\partial x} \quad (21)$$

The relative importance of the pressure gradient $-g\partial H/\partial x$ is not easy to estimate. Negretti, et al. [33] argues that the pressure change is dependent on the flow-blockage ($C_D a D$). For a solid cylinder (SVF=1.0), there is a drop of the local water depth, H , directly behind the body, and H then approaches H_∞ in the wake, i.e. $\partial H/\partial x > 0$. Consequently, all terms on the right of Eq. (21) are negative, which results in a negative value of r . For medium dense patches ($0.03 < \text{SVF} < 0.15$), the length of steady wake has a lower limit, $L_1 \geq 2.5D$, and L_1 increases as SVF decreases [14]. Assuming that $D/2L_1 \ll 1$, then

$$\frac{2U_{1s}}{U} r \sim -\left(\frac{U_{1s}}{U}\right)^2 S - \frac{2gD}{U^2} \frac{\partial H}{\partial x} \quad (22)$$

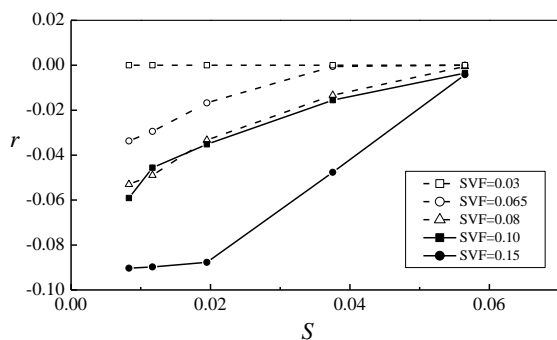


Fig. 17 Dependence of steady wake on bed friction.

For a given SVF, the value of U_{1s} was almost constant (Fig. 5). Thus, Eq. (22) approximates a linear relationship between r and S , which is shown in Fig. 17. As L_1 appears in the denominator in Eq.(20), a small value was assigned to L_1 to avoid singularity when plotting Fig. 17. Having that $U_{1e} \leq U_{1s}$, the value of r was negative, which also indicated that the pressure gradient overwhelmed the bed friction in the steady wake. For a sparse patch (SVF = 0.03), r was 0, suggesting that streamwise velocity in the steady wake was constant. For a mid-dense patch ($0.03 < \text{SVF} < 0.15$), r increased monotonously with S . This upward trend did not cease until r reached 0. However, the increasing trend was not explicitly shown in Eq.(22), which indicated that the last term in Eq. (22) may be implicitly related to S . For a highly-dense patch (SVF = 0.15), the pressure gradient was so strong that r was nearly constant when $S < 0.02$ and increased when $S >$

0.02. In addition, Fig. 17 provided insight into the relative levels of the pressure gradient of different patches. As S got very small, the bed friction became negligible (from Eq.(21)). As a result, r was only related to the pressure gradient. Therefore, the pressure gradient $\partial H/\partial x$ for a denser patch was higher than a sparser patch in the steady wake.

4. Conclusions

Numerical simulations of shallow water flow through and around a patch of emergent cylinders were conducted with combinations of different patch density (SVF) and water depth (H). The flow velocity at the leading edge of the patch was found to depend on SVF only. Within the patch, there was a reduction of turbulent kinetic energy (TKE) due to bed friction at small water depths H .

Behind the patch, the steady wake was found to not only depend on the patch density but also on the bed friction. The streamwise velocity at the starting point of the steady wake, or the velocity exiting the patch U_{1s} , the velocity at the end of the steady wake U_{1e} , and the length of the steady wake L_1 were used to describe the steady wake. The stability parameter, S , was adopted to characterize bed friction. The magnitude of U_{1s} decreased with SVF increasing (SVF < 0.15), and appeared to be unaffected by S . Nevertheless, the values of U_{1e} and L_1 were affected by both SVF and S . For a sparse patch (SVF = 0.03), U_{1e} was equal to U_{1s} and L_1 decreased as S increased. For a mid-dense patch ($0.03 < \text{SVF} < 0.15$), U_{1e} was smaller than U_{1s} and gradually increased to U_{1s} when S increased. The velocity difference between U_{1e} and the velocity outside the steady wake determined the development of the SSLs, hence the length of the steady wake. Indeed, L_1 decreased with the increase of S until U_{1e} increased to U_{1s} . For a highly-dense patch (SVF = 0.15), U_{1e} was still smaller than U_{1s} , but it remained constant unless S was greater than 0.02. The same trend was found for the variation of L_1 . Besides, the steady wake was ill-defined when U_{1e} exceeded U_{1s} as it was difficult to distinguish the steady wake from the velocity profiles.

Behind the steady wake, the patch-scale turbulence existed as a result of the interaction between two SSLs formed at the shoulders of the patch. The patch-scale turbulence was also suppressed by bed friction. As S increased, the turbulence level reduced, and the patch-scale vortex was elongated. Moreover, the Strouhal number associated with the wake oscillation increased.

Based on the shallow water equations and the restrictions of the steady wake, a reduced dimensionality model was derived to analyze the

steady wake. A new parameter, r , was proposed to describe the development rate of the steady wake. The numerical results showed that r increased monotonously with S for mid-dense patches ($0.03 < SVF < 0.15$).

References

- [1] Wilcock Robert J., Champion Paul D., Nagels John W., Croker Glenys F. The influence of aquatic macrophytes on the hydraulic and physico-chemical properties of a New Zealand lowland stream [J]. *Hydrobiologia*, 1999, 416(0): 203-214.
- [2] Huai W. X., Wang W. J., Hu Y., Zeng Y. H., Yang Z. H. Analytical model of the mean velocity distribution in an open channel with double-layered rigid vegetation [J]. *Advances in Water Resources*, 2014, 69: 106-113.
- [3] Yang Zhong-Hua, Bai Feng-Peng, Huai Wen-Xin, Li Cheng-Guang. Lattice Boltzmann method for simulating flows in open-channel with partial emergent rigid vegetation cover [J]. *Journal of Hydrodynamics*, 2019, 31(4): 717-724.
- [4] Ai Y. D., Liu M. Y., Huai W. X. Numerical investigation of flow with floating vegetation island [J]. *Journal of Hydrodynamics*, 2020, 32(1): 31-43.
- [5] Liang D. F., Wu X. F. A random walk simulation of scalar mixing in flows through submerged vegetations [J]. *Journal of Hydrodynamics*, 2014, 26(3): 343-350.
- [6] Huai Wen-Xin, Zhang Jiao, Katul Gabriel G, Cheng Yong-Guang, Tang Xue, Wang Wei-Jie. The structure of turbulent flow through submerged flexible vegetation [J]. *Journal of Hydrodynamics*, 2019, 31(2): 274-292.
- [7] Rominger J. T., Lightbody A. F., Nepf H. M. Effects of Added Vegetation on Sand Bar Stability and Stream Hydrodynamics [J]. *Journal of Hydraulic Engineering*, 2010, 136(12): 994-1002.
- [8] Nepf Heidi M. Hydrodynamics of vegetated channels [J]. *Journal of Hydraulic Research*, 2012, 50(3): 262-279.
- [9] Rowiński Paweł, Radecki-Pawlik Artur. *Rivers – Physical, Fluvial and Environmental Processes* [M]. Switzerland: Springer, 2015.
- [10] Sand-Jensen K., Pedersen M. L. Streamlining of plant patches in streams [J]. *Freshwater Biology*, 2008, 53(4): 714-726.
- [11] Nepf Heidi M. Flow and Transport in Regions with Aquatic Vegetation [J]. *Annual Review of Fluid Mechanics*, 2012, 44(1): 123-142.
- [12] Zong L. J., Nepf H. Vortex development behind a finite porous obstruction in a channel [J]. *Journal of Fluid Mechanics*, 2012, 691: 368-391.
- [13] Ball D J, Allison N., Stansby P K. Modeling shallow water flow around pile groups [J]. *Ice Proceedings Water Maritime & Energy*, 1996, 118(4): 226-236.
- [14] Chen Z. B., Ortiz A., Zong L. J., Nepf H. The wake structure behind a porous obstruction and its implications for deposition near a finite patch of emergent vegetation [J]. *Water Resources Research*, 2012, 48(9).
- [15] Chang Kyoungsik, Constantinescu George. Numerical investigation of flow and turbulence structure through and around a circular array of rigid cylinders [J]. *Journal of Fluid Mechanics*, 2015, 776: 161-199.
- [16] Nicolle A., Eames I. Numerical study of flow through and around a circular array of cylinders [J]. *Journal of Fluid Mechanics*, 2011, 679(7): 1-31.
- [17] Chen D. Y., Jirka G. H. Absolute and convective instabilities of plane turbulent wakes in a shallow water layer [J]. *Journal of Fluid Mechanics*, 1997, 338: 157-172.
- [18] Lam M. Y., Ghidaoui M. S. Fourier analysis of the roll-up and merging of coherent structures in shallow mixing layers [J]. *Environmental Fluid Mechanics*, 2014, 14(5): 997-1026.
- [19] Ingram R. G., Chu V. H. Flow around Islands in Rupert Bay - an Investigation of the Bottom Friction Effect [J]. *Journal of Geophysical Research-Oceans*, 1987, 92(C13): 14521-14533.
- [20] Chu V. H., Wu J. - H., Khayat R. E. Stability of Transverse Shear Flows in Shallow Open Channels [J]. *Journal of Hydraulic Engineering*, 1991, 117(10): 1370-1388.
- [21] Lam M. Y., Ghidaoui M. S., Kolyshkin A. A. Hydraulics of shallow shear flows: onset, development and practical relevance [J]. *Environmental Fluid Mechanics*, 2019, 19(5): 1121-1142.
- [22] Chu Vincent H, Babarutsi Sofia. Confinement and bed-friction effects in shallow turbulent mixing layers [J]. *Journal of Hydraulic Engineering*, 1988, 114(10): 1257-1274.
- [23] Phillips N. A. A coordinate system having some special advantages for numerical forecasting [J]. *Journal of Meteorology*, 1957, 14(2): 184-185.
- [24] Menter F. Zonal two equation kw turbulence models for aerodynamic flows [C]. 23rd Fluid Dynamics, Plasmadynamics, and Lasers Conference, 6-9 July, 1993, Orlando, Florida, USA.
- [25] Zhang J. X., Wang J., Fan X., Liang D. F. Numerical investigation of water wave near-trapping by rigid emergent vegetation [J]. *Journal of Hydro-environment Research*, 2019, 25: 35-47.
- [26] Takemura T., Tanaka N. Flow structures and drag characteristics of a colony-type emergent roughness model mounted on a flat plate in uniform flow [J]. *Fluid Dynamics Research*, 2007, 39(9-10): 694-710.
- [27] Rominger J. T., Nepf H. M. Flow adjustment and interior flow associated with a rectangular porous obstruction [J]. *Journal of Fluid Mechanics*, 2011, 680: 636-659.
- [28] Nepf Hm, Sullivan Ja, Zavistoski Ra. A model for diffusion within emergent vegetation [J]. *Limnology and Oceanography*, 1997, 42(8): 1735-1745.
- [29] Chang W. Y., Constantinescu G., Tsai W. F. On the flow and coherent structures generated by a circular array of rigid emerged cylinders placed in an open channel with flat and deformed bed [J]. *Journal of Fluid Mechanics*, 2017, 831: 1-40.
- [30] Chang K., Constantinescu G., Park S. 2-D eddy resolving simulations of flow past a circular array of cylindrical plant stems [J]. *Journal of Hydrodynamics*, 2018, 30(2): 317-335.
- [31] Zhang J. X., Liang D. F., Fan X., Liu H. Detached eddy simulation of flow through a circular patch of free-surface-piercing cylinders [J]. *Advances in Water Resources*, 2019, 123: 96-108.
- [32] Chen D. Y., Jirka G. H. Experimental-Study of Plane Turbulent Wakes in a Shallow-Water Layer [J]. *Fluid Dynamics Research*, 1995, 16(1): 11-41.
- [33] Negretti M. E., Vignoli G., Tubino M., Brocchini M. On shallow-water wakes: an analytical study [J]. *Journal of Fluid Mechanics*, 2006, 567: 457-475.